Research article

Elucidation of fibril structure responsible for swimming in *Spiroplasma* using electron microscopy

Yuya Sasajima[a], Takayuki Kato[b], Tomoko Miyata[c], Keiichi Namba[c,d,e] and Makoto Miyata[a,f]

[a]Graduate School of Science, Osaka City University, Osaka, 558-8585, Japan, [b]Institute for Protein Research, Osaka University, 3-2 Yamadaoka, Suita, Osaka, 565-0871, Japan, [c]Graduate School of Frontier Biosciences, Osaka University, 1-3 Yamadaoka, Suita, Osaka, 565-0871, Japan, [d]RIKEN Center for Biosystems Dynamics Research and SPring-8 Center, 1-3 Yamadaoka, Suita, Osaka, 565-0871, Japan, [e]JEOL YOKOGUSHI Research Alliance Laboratories, Osaka University, 1-3 Yamadaoka, Suita, Osaka, 565-0871, Japan, [f]The OCU Advanced Research Institute for Natural Science and Technology (OCARINA), Osaka City University, Osaka, 558-8585, Japan.

Address correspondence to Makoto Miyata, miyata@sci.osaka-cu.ac.jp

Author Contributions: YS and MM designed the research. YS performed the research. TK, TM, and KN provided techniques for structural analyses. YS, KN, and MM wrote the paper. All authors discussed and checked the entire manuscript.

Competing Interest Statement: The authors have no competing interests to declare.

Classification: Major class: Biological Science. Minor class: Microbiology; Biophysics and Computational Biology.

Keywords: Single particle analysis, Helical shape, Motility, Cytoskeleton, Filament.

Abstract

Spiroplasma, known pathogens of arthropods and plants, are helical-shaped bacteria lacking the peptidoglycan layer. They swim by alternating between left- and right-handed cell helicity, which is driven by an internal structure called the ribbon. This system is unrelated to flagellar motility that is widespread in bacteria. The ribbon comprises the bacterial actin homolog MreB and fibril, the protein specific to *Spiroplasma*. Here, we isolated the ribbon and its core, the fibril filament, and using electron microscopy, found that the helicity of the ribbon and the cell is linked to the helicity of the fibril. Single particle analysis using the negative-staining method revealed that the three-dimensional structures of the fibril filament comprise a repeated ring structure twisting along the filament axis. Based on these observations, we propose a scheme for the helicity-switching mechanism in which the twists caused by the conformational changes in the fibril filament are accumulated, transmitted to the ribbon, and then propel the cells by rotating the cell body like a screw.

Significance Statement

Spiroplasma are widespread globally as pathogens of animals and plants. They are also recognized as male-killing bacteria of insects. Their special swimming mechanism is caused by helicity switching, which could be the simplest swimming mechanism. This mechanism has attracted research attention for many years because of the possible application in the field of nano actuators; however, the details of this mechanism remain to be clarified. Here, we reveal the outline of the swimming mechanism by analyzing the structure of the core of the *Spiroplasma* ribbon.

Introduction

Mollicutes, which are parasitic or commensal bacteria, have evolved from the phylum Firmicutes that includes *Bacillus* and *Clostridium* by reducing their genome sizes (1). In the course of evolution, the cells have become softer and smaller owing to the loss of the peptidoglycan layer, allowing them to transmit their internal housekeeping activities to the outside, resulting in the acquisition of three unique motility mechanisms (1). Two of the three, represented by *Mycoplasma mobile* and *Mycoplasma pneumoniae*, exhibit gliding motilities on solid surfaces in which leg structures repeatedly catch sialylated oligosaccharides on host cells, based on two different mechanisms (2-4). The other motility system is the helicity-switching swimming of *Spiroplasma*, the subject of the present study (Movie_S1) (2, 5-7). *Spiroplasma* species are

parasitic to plants and arthropods, and are characterized as polarized helical-shaped cells with a tapered end (8, 9). They also show obvious chemotaxis despite the absence of genes for the two-component regulatory system in the genome, which is generally responsible for bacterial chemotaxis (10). In general, swimming bacteria such as *Escherichia coli*, *Salmonella*, and spirochetes can migrate by the rotational motion of the flagellar motor fixed to the peptidoglycan layer, whereas *Spiroplasma* have a unique swimming system in which kinks propagate along the cell body with a switch between left-handed and right-handed cell helicity (Fig. 1A). This swimming is driven by an intracellular structure called the "ribbon" which localizes along the innermost line of the helical cell structure, and structural changes in the ribbon may switch the cell helicity (11, 12). Therefore, the detailed structure of the ribbon should be elucidated to determine this swimming mechanism.

In previous studies using electron microscopy, two types of filaments in the ribbon were visualized (11, 12). One comprises a protein "fibril," specific to *Spiroplasma*. The other is possibly MreB, the bacterial actin homolog (10-12). As *Spiroplasma* MreBs are distantly located from other MreBs in the phylogenetic tree, here, we use the term SMreB (13, 14). Fibril protein has been studied as a linear motor protein which is responsible for the helicity-switching (15, 16). The fibril filament is considered to function as a chain of elliptical rings. However, the structure and function of the fibril protein remains unclear.

In the present study, we clarified the structure of the fibril filament, which is unrelated to that of any other known cytoskeletal filament, using electron microscopy (EM) and single particle analysis. Then, we proposed a scheme for the helicity-switching swimming of *Spiroplasma*.

Results

Cell helicity is derived from the internal ribbon structure

To clarify which structure forms the helical cell morphology of *Spiroplasma*, we first measured the helical pitches of the swimming cells using optical microscopy. The helical shape of the cells can be observed as a series of density segments in the defocused image plane, relative to the cell axis under phase contrast microscopy (Fig. 1B). The helical pitches between the left- and right-handed segments along the cell axis were 696 ± 32 (n = 159) and 697 ± 37 nm (n = 146), respectively. Next, we performed EM to analyze the internal ribbon structure to compare the helical pitches of the cells and the ribbons. The cells were bound to EM grids non-specifically, chemically fixed by glutaraldehyde, and then stained

with uranyl acetate. Negative-staining EM showed the images of helical-shaped cells with a narrow tip at one side (Fig. 1C). Next, we exposed the internal ribbon structure by treating the cells with 0.1% Triton X-100 on the grid (Fig. 1D). The ribbon showed a “spiral” flat structure comprising protofilaments. However, generally, in negative-staining EM, the specimens are placed in vacuum and dried and can result in distortions, which is disadvantageous for helix observation. Therefore, we applied quick-freeze, deep-etch (QFDE) EM to visualize the structure as close to the original as possible. In QFDE, a sample is frozen in milliseconds, exposed by fracturing and etching, and then a platinum replica is made by shadowing. The observation of the replica by transmission EM gives subnanometer resolution images with high contrast (17, 18). The cells were non-specifically bound to mica flakes and fixed by quick freezing in a liquid condition. Then, we prepared replicas by fracturing and platinum coating. QFDE-EM showed cell morphology consistent with the results from negative-staining EM (Fig. 1E). Using QFDE-EM, we also observed the ribbon exposed with 0.1% Triton X-100 treatment (Fig. 1F). The ribbon showed the “helicoid” structure in which the twisted positions were aligned in a line. When the cells were starved in phosphate-buffered saline (PBS) without glucose for 30 min, they all showed a left helix with the same pitch. Therefore, we assumed that this structure is the default state of the cell. Table 1 summarizes parameters that present the helicity of cells and ribbons obtained with the two EM methods (Fig. 1G, H). The helical pitches of the cells and the ribbons were in good agreement, indicating that the ribbon forms the cell helicity. As the helix diameter of the ribbon was one-third that of the cell helix, the ribbon should be localized along the innermost line of the cell helix.

Characterization of the isolated ribbon

We intended to use A22, an inhibitor of MreB polymerization to examine the role of MreBs in the ribbon (Fig. 2A) (19), because the binding of A22 to SMreBs has been suggested from amino acid sequences (13). First, we examined the effect of 1 mM A22 on swimming *Spiroplasma* cells (Movie_S2). The cells shifted to a right-handed helix form and stopped moving in 2 min (Fig. 2B a, b), suggesting that the functions of SMreBs are also inhibited by A22. The resulting helical pitches of the cells were distributed around a peak at 426 ± 47 nm, shorter than the original (Fig. 2B c).

The cell suspension was treated with 1% Triton X-100 and subjected to stepwise gradient centrifugation, consisting of 0%, 20%, 30%, 40%, 50%, and 60% sucrose layers. After centrifugation, we found a dense layer of cell contents at the bottom of the 40% sucrose layer. We recovered and observed the fraction

under EM and found that the ribbon comprised protofilaments with a width of 66 ± 12 nm and length longer than 2 μm (Fig. 2C a). The ribbons were twisted with a pitch of 350 ± 17 nm (n = 47) (Fig. 2D a) consistent with the helical pitches of the cells and the ribbons prepared on the grid (Fig. 1, Table 1) ($P = 0.7 > 0.01$). To analyze the number and width of the protofilaments involved in the isolated ribbon, we traced a sectional image profile of the ribbon (Fig. 2D b). Six to nine protofilaments were detected with widths ranging between 4–16 nm (Fig. 2D c, d and Fig. S1). SDS-PAGE analysis of this fraction showed five protein bands including six proteins (Table 2). The band (v) contained SMreBs 2 and 4. The whole ribbon fraction mainly comprised fibril protein and the SMreBs 2 and 4 with an intensity ratio of 47% and 37%, respectively (Fig. 2E).

Next, we examined the effects of A22 on the ribbon. We kept cells in 1 mM A22 for 2.5 h at 30 °C and observed the ribbon. The ribbons were observed in a dispersed form with width distribution characterized by three peaks, 9.5, 15.0, and 22.2 nm (Fig. 2C c, D d). SDS-PAGE analysis clarified the content as 67% and 11% for fibril and SMreB proteins, respectively (Fig. 2E), suggesting that the protofilaments comprising fibril protein are bundled by SMreBs in the ribbon structure.

Helical pitch of the isolated fibril filament

To analyze the detailed structure, we treated the ribbon fraction with cholic acid and isolated the fibril protein using sucrose-gradient centrifugation. SDS-PAGE analysis showed that the fraction contains only fibril protein (Fig. 3A). We examined the ATPase activity of fibril protein by monitoring phosphate release because we expect ATP as the direct energy source for *Spiroplasma* swimming. Fibril protein at 17 μM was mixed with 2 mM ATP in the presence of Mg ions, but phosphate was not released even after 250 min at 30 °C. Then, we concluded that the fibril protein does not have the obvious ATPase activity. Negative-staining EM showed that the fibril protein forms filaments which include single- and double-stranded filaments and bundles, suggesting various types of interactions between fibril protein molecules (Fig. 3B a). A single-stranded fibril filament consisted of repeated ring units approximately 10 nm long (Fig. 3B b) and 7 nm wide as observed in the side view (Fig. 3B c). A double-stranded fibril filament appeared to be formed by aligning two single-stranded filaments to face each other at the side of the ring, resulting in a thickness and width of 14 nm and 7 nm, respectively (Fig. 3B d), forming a 10 nm long repeating structure. We analyzed the helical pitches for the double-stranded fibril filaments, because the double-stranded fibril filament had enough persistent length to cover the helical pitch with a clear twist of the ring pattern along the filament axis. The images of

the fibril filament cropped from the electron micrographs using the straightening selection tool of ImageJ software were subjected to a fast Fourier transform (FFT) to remove noise, and then, the generated image was subjected to an inverse FFT (Fig. 3C). To ensure that the FFT images did not include artificial mistakes, we also generated the two-dimensional (2D) averaged images from 312 randomly picked particles with a box size of 45 nm along the filament axis using RELION 3.0 software (Fig. 3D)(20). The three classes of images corresponded well to different positions of the filament images generated by FFT, suggesting that the FFT images reflect the original structures. The helical pitch estimated from the FFT images was 343 ± 22 nm (n = 158) (Fig. 3G a). However, we could not conclude the handedness of the fibril filament, because the alignment of the filament on the EM grid was not distinguishable with negative-staining EM. Therefore, we analyzed the isolated fibril filament using QFDE-EM (Fig. 3F) because the replica is made by platinum, which is not transparent to an electron beam. We succeeded in the determination of their handedness (Fig. 3F) and concluded that the double-stranded fibril filament forms a left-handed helix with a pitch distribution of 351 ± 33 nm (n = 50) (Fig. 3G b). The helix features were consistent with the pitch of the cell in the default state and that of the isolated ribbon (Table 1), suggesting that the fibril pitch is the determinant for the pitch of the ribbon and cell.

Three-dimensional reconstruction of fibril filaments

To detect the conformational changes in the fibril three dimensionally, we performed single particle analysis based on negative-staining EM. The double-stranded fibril filament was not suitable for image averaging owing to the positional variety in the binding of the two filaments (Fig. 3 and Fig. S2). Therefore, we sonicated the purified fibril fraction to increase the proportion of single-stranded forms and succeeded in the acquisition of single-stranded images (Fig. 4A). From the selected 11 867 particles with good quality, the 2D-averaged images were summarized into three types (i), (ii), and (iii) (Fig. 4A b). Then, the initial 3D model was reconstructed using the *ab-initio* 3D function of cisTEM software (21) and used as the reference for the following 3D classification (Fig. 4A c). Three dimensional structures of the fibril filament reconstructed from the total of 11 867 particles by RELION 3.0 software showed three conformations, i.e., class 1: left-handed mostly straight (49%), class 2: left-handed with curvature (24%), and class 3: right-handed with curvature (27%) (Fig. 4A d and Fig. S3). Two dimensional re-projections from these three structures corresponded well to the 2D class averages, indicating the validity of the obtained 3D structures (Fig. S4). The 3D structure of the fibril filament had repeating elliptical rings with a pitch of 8.7 nm along the filament axis, with long

and short axes of 11 and 6 nm, respectively. A short cylinder connects the ring units causing a positive curvature (Fig. 4A d). These characteristics were common to all three classes. Cross-sectional images perpendicular to the longitudinal axis of the filament showed a “boomerang-like shape”, which had a dent at one side and protrusion at the other (Fig. 4B). We evaluated the twist of the fibril filament around the filament axis by measuring the directions of the Feret diameter, the longest diagonal line of cross-sectional images. Fibril filaments twisted along the filament axis. The twisting angles were estimated from the angle averages of the first and fourth units, as 4.8 (left-handed), 7.6 (left-handed), and 5.9 (right-handed) degrees for classes 1, 2, and 3, respectively. Although superimposition of classes 2 and 3 showed diagonal shifts between these two conformations, the positions responsible for the structural shift could not be identified owing to the low resolution of structures (Fig. 4C). We constructed long filament models representing a helical pitch by stacking the ring units (Fig. 4D). Class 1 formed a left-handed helix with a diameter of 280 nm and a pitch of 530 nm. Class 2 formed the left-handed helix with a diameter of 110 nm and a pitch of 210 nm. Class 3 formed the right-handed helix with a diameter of 110 nm and a pitch of 310 nm. We attempted to reconstruct the double stranded filaments through image averaging and failed (Fig. S2). It is likely caused by the variation in binding positions in the formation of the double strand. We reconstructed the double strand from the structure of the single-stranded filament (Fig 3E), which was consistent with the images obtained using the other methods.

Assignment of the predicted fibril protein structure to a density map

To predict the fibril structure, we searched for template structures for homology modeling using SWISS-MODEL and obtained the methylthioadenosine/S-adenosylhomocysteine (MTA/SAH) nucleosidase of *Bacillus anthracis* (PDB ID: 4QEZ) (22), which has a 25.6% amino acid sequence identity to the N-terminal region amino acid residues 1–228 of the fibril protein. In contrast, the sequence of the C-terminal region of amino acids 229–512 did not show significant homology with other proteins in the BLAST search using non-redundant protein sequences (searched on December 24, 2020). These results are consistent with a previous observation in 2011 (15). Then, we assumed that the fibril protein can be divided into the N-terminal domain, comprising amino acid residues 1–228 and the remaining portion. Secondary-structure prediction based on the amino acid sequences showed similarity between the N-terminal domain of the fibril protein and *B. anthracis* MTA/SAH nucleosidase (Fig. 5A), suggesting the similarity also in 3D structures. Therefore, we used *B. anthracis* MTA/SAH nucleosidase as a template for the homology modeling of the N-terminal region

of the fibril protein using SWISS-MODEL. The predicted model showed a homodimer in which the monomers interact with each other to occlude a hydrophobic surface, as observed in the crystal structure of *B. anthracis* MTA/SAH nucleosidase (Fig. 5B). The predicted rod-shaped dimer had dimensions of 75, 60, and 50 Å. We then manually searched for the position in the density map from EM to assign the predicted molecular model (Fig. 5C). The predicted rod structure could be assigned to only one position, because it was too thick to assign to the other positions. The gap between the two subunits of the predicted structure fit to a gap observed in the density map from EM. Based on these results, we determined the alignment of the subunits in the protofilament (Fig. 5D).

Discussion

Fibril and ribbon structures

Although the interconnected ring structure in the fibril filament has been observed (10, 15), the 3D reconstruction of the fibril has not been achieved to date. In the present study, we clarified the 3D structure of the fibril filament for the first time. The sonication in the isolation process was effective in isolating the single stranded filament, whose uniform structure was advantageous for image averaging (Fig. 4). The structure determined here showed a width of 10.5 nm, and was in good agreement with the corresponding filament structure obtained through electron cryotomography (12), suggesting that the filaments isolated here retained the original structure. The left-handed conformation accounted for 73% of the fibril filament, suggesting that this conformation is more stable than others. This observation may explain the fact that both the cells in a default state and the isolated ribbons were mostly left-handed (23, 24). The fibril structure is likely more stable in the left-handed conformation than in the right-handed one. The fibril filament did not show any polarity along the filament axis, although *Spiroplasma* cells swim in a directed manner (Fig. 1) (5, 10). This directionality could be caused by structures other than the fibril, for example, SMreB proteins and the dumbbell formed at the cell front (10, 14, 25). We obtained three different filament conformations with different curvatures, in other words, the helix diameter. This variety in curvature may function in directing the ribbon formation, in which the filament at the ribbon edges requires a longer helix diameter than those at the central positions (Fig. 6).

Swimming mechanism

Based on these results, we can now suggest the core part of the helicity-

switching mechanism (Fig. 6). The ribbon comprises 6–9 fibril filaments connected laterally and oriented along the innermost part of the helical cell (Fig. 6A). The fibril should support the cell membrane through their ring structures, because the fibril filament has a positive curvature toward the backbone (Fig. 6B a upper). Thus, the fibril twist forms the twist of the ribbon and the cell with the same handedness, because the fibril filament binds to the adjacent filaments through their fixed positions (Fig. 6B a lower). If the fibril filaments in the ribbon have strong cooperativity along the ribbon axis and transmit the twist to the next levels, the helicity shift travels along the ribbon axis, with accumulation of the rotational angle (Fig. 6B b) (23). If we assume that such a ribbon is fixed at a tip on the front end, then, the shift initiated at the tip travels backward, along with rotation of the back portion to release the torsion, in a direction that pushes water backward (Fig. 6C) (Movie_S1). The ribbon structure drives the cell structure and propels the cell forward by pushing water backward like a screw.

Possible molecular mechanism for helicity-switching

The N-terminal region of the fibril protein has an amino acid sequence identity of as much as 25.6% with MTA/SAH nucleosidase from a bacterial species, *B. anthracis*. This protein is essential for bacterial growth because it recycles adenine and methionine through S-adenosylmethionine (SAM)-mediated methylation reactions and produces the universal quorum-sensing signal, autoinducer-2 (AI-2) (26). The fibril protein probably evolved from this protein, which is abundant in a cell, by acquiring a C-terminal region possessing polymerization activity. Class Mollicutes lack the respiration pathway to generate membrane potential and produce ATP through glycolysis and arginine fermentation (27). Therefore, the energy for swimming should also be supplied by ATP, rather than the membrane potential, because the energy required for growth is supplied by ATP, which is produced by glycolysis in *Spiroplasma*. In fact, the two motility mechanisms of Mollicutes genus, *Mycoplasma mobile*-type and *Mycoplasma pneumoniae*-type gliding mechanisms depend on the hydrolytic energy of ATP (28-31). The fibril protein derived from the MTA/SAH nucleosidase is unlikely to have ATPase activity, and no ATPase activity was detected in the fibril fraction. These facts suggest that other proteins may be involved in the helicity switching (12, 14, 32). The ribbon contains SMreB proteins, and interestingly, most genomes of the *Spiroplasma* code for five classes of SMreBs (13, 14, 33). Moreover, in the present study, we showed that SMreBs have roles to bundle fibril filaments (Fig. 2 C). Generally, MreBs exhibit polymerization dynamics based on ATP hydrolysis, and function to assign peptidoglycan synthesizing complexes (1, 17, 19, 34) and as a rail for the gliding motor of *Myxococcus xanthus* (35). SMreB5, a member in the five classes, is known to be

essential for helix formation and swimming of *Spiroplasma citri* cells (14). These facts suggest that SMreBs support and drive the helices formed by the fibril. Perhaps, SMreB itself also forms filamentous structures along the cell axis (11, 12). In fact, MreB-like filaments have been observed along the cell axis by EM analyses of *Spiroplasma melliferum* (12).

Materials and Methods

Bacterial strains and culture conditions

The type strain, TDA-040725-5^T, of *Spiroplasma eriocheiris* was cultured in R2 medium (2.5% [wt/vol] heart infusion broth, 8% sucrose, and 10% horse serum) at 30 °C to an optical density of 0.06 to 0.1 at 600 nm (10, 36).

Optical microscopy

Cultured cells were centrifuged at 11 000 × *g*, 10 °C for 10 min and suspended in PBS consisting of 75 mM sodium phosphate [pH 7.3], 100 mM NaCl, containing 20 mM glucose and 0.6% methylcellulose to be of a cell density 10-fold higher than that of the original (10, 36). The cells were inserted into a tunnel chamber assembled by taping coverslips as previously described and observed under an IX71 microscope (Olympus, Tokyo, Japan) (37). The video was captured using a DMK33UX174 complementary metal–oxide–semiconductor (CMOS) camera (The Imaging Source, Taipei, Taiwan) and analyzed using ImageJ v1.53a (https://imagej.nih.gov/ij/).

Electron microscopy

To observe the intact cells, the cell suspension was placed on a hydrophilized grid, fixed using 2% glutaraldehyde, washed with water, and stained with 2% uranyl acetate. To observe the internal structure, the cell suspension on a grid was treated with PBS including 0.1 mg/mL DNase and 1 mM $MgCl_2$ for 20 s, and washed and stained with 2% uranyl acetate. QFDE-EM was performed as previously reported for specimens suspended with mica flakes (17). The images were acquired using a JEM1010 EM (JEOL, Akishima, Japan) equipped with a FastScan-F214(T) charged-coupled device (CCD) camera (TVIPS, Gauting, Germany) and analyzed using ImageJ v1.53a.

Isolation of ribbon and fibril

To isolate the internal structure, 10 mL of cell suspension in PBS was treated with 1% Triton X-100, 0.1 mg/mL DNase, 1 mM $MgCl_2$, and 0.1 mM PMSF with shaking for 10 min at 4 °C. The insoluble fraction was recovered by centrifugation

at 20 000 × *g*, 4 °C for 30 min and suspended in PBS to be 0.2 mL. The sample was laid at the top of sucrose solution layers of 0%, 20%, 30%, 40%, 50%, and 60%, and centrifugated at 20 000 × *g*, 4 °C for 20 min in a 1.5 mL tube with a fixed angle. To isolate the fibril filament, the insoluble fraction was additionally treated with a solution consisting of 2% choric acid, 20 mM Tris-Cl pH 8.0, 150 mM NaCl at 4 °C for 8 h and subjected to stepwise density gradient centrifugation.

ATPase assay

ATPase activity was assayed by a continuous spectrophotometric method using a 2-amino-6-mercapto-7-methylpurine ribonucleoside–purine nucleoside phosphorylase reaction to detect the released inorganic phosphate at 30 °C (EnzChek kit; Life Technologies, Carlsbad, CA, USA). The reaction mixture was as follows: 17 μM purified fibril filament, 1 mM $MgCl_2$, 20 mM Tris-HCl (pH 7.5) in a total volume of 0.2 mL (38).

Reconstitution of 3D structure

The contrast transfer function (CTF) parameters for negative-staining EM images were estimated using Gctf25 software (39). The images of fibril filaments were selected automatically by RELION 3.0 (20) as helical objects and segmented as squares of 200 × 200 pixels with 90% overlap. These 14 543 images were 2D-classified and 11 867 images were selected for further analyses. *ab-initio* reconstitution was performed by cisTEM (21) based on segmented images from 12 classes. The selected 11 867 particle images were 3D-classified using the 3D map in RELION 3.0 (20).

Acknowledgments

We thank Yuhei O Tahara, Daichi Takahashi, Hana Kiyama, and Ikuko Fujiwara at the Graduate School of Science, Osaka City University, Japan for helpful discussions. This study was supported by a Grants-in-Aid for Scientific Research A (MEXT KAKENHI, Grant Number JP17H01544), JST CREST (Grant Number JPMJCR19S5), the Osaka City University (OCU) Strategic Research Grant 2017 for top priority researches to MM, and JSPS KAKENHI (Grant Number JP25000013), the Platform Project for Supporting Drug Discovery and Life Science Research (BINDS) from AMED (Grant Number JP19am0101117 and support number 1282), the Cyclic Innovation for Clinical Empowerment (CiCLE) from AMED (Grant Number JP17pc0101020), and JEOL YOKOGUSHI Research Alliance Laboratories of Osaka University to KN.

References

1. Miyata M, *et al.* (2020) Tree of motility - A proposed history of motility systems in the tree of life. *Genes Cells* 25(1):6-21.
2. Miyata M & Hamaguchi T (2016) Integrated information and prospects for gliding mechanism of the pathogenic bacterium *Mycoplasma pneumoniae*. *Front Microbiol* 7:960.
3. Miyata M & Hamaguchi T (2016) Prospects for the gliding mechanism of *Mycoplasma mobile*. *Curr Opin Microbiol* 29:15-21.
4. Miyata M (2010) Unique centipede mechanism of *Mycoplasma* gliding. *Annu Rev Microbiol* 64:519-537.
5. Harne S, Gayathri P, & Beven L (2020) Exploring *Spiroplasma* biology: opportunities and challenges. *Front Microbiol* 11:589279.
6. Wada H & Netz RR (2009) Hydrodynamics of helical-shaped bacterial motility. *Phys Rev E Stat Nonlin Soft Matter Phys* 80(2 Pt 1):021921.
7. Shaevitz JW, Lee JY, & Fletcher DA (2005) *Spiroplasma* swim by a processive change in body helicity. *Cell* 122(6):941-945.
8. Harumoto T & Lemaitre B (2018) Male-killing toxin in a bacterial symbiont of *Drosophila*. *Nature* 557(7704):252-255.
9. Gasparich GE (2002) *Spiroplasmas*: evolution, adaptation and diversity. *Front Biosci* 7:d619-640.
10. Liu P, *et al.* (2017) Chemotaxis without conventional two-component system, based on cell polarity and aerobic conditions in helicity-switching swimming of *Spiroplasma eriocheiris*. *Front Microbiol* 8:58.
11. Trachtenberg S, *et al.* (2008) Structure of the cytoskeleton of *Spiroplasma melliferum* BC3 and its interactions with the cell membrane. *J Mol Biol* 378(4):778-789.
12. Kurner J, Frangakis AS, & Baumeister W (2005) Cryo-electron tomography reveals the cytoskeletal structure of *Spiroplasma melliferum*. *Science* 307(5708):436-438.
13. Takahashi D, Fujiwara I, & Miyata M (2020) Phylogenetic origin and sequence features of MreB from the wall-less swimming bacteria *Spiroplasma*. *Biochem Biophys Res Commun* 533(4):638-644.
14. Harne S, *et al.* (2020) MreB5 Is a determinant of rod-to-helical transition in the cell-wall-less bacterium *Spiroplasma*. *Curr Biol* 30(23):4753-4762.e4757.
15. Cohen-Krausz S, Cabahug PC, & Trachtenberg S (2011) The monomeric, tetrameric, and fibrillar organization of Fib: the dynamic building block of the bacterial linear motor of *Spiroplasma melliferum* BC3. *J Mol Biol* 410(2):194-213.
16. Townsend R, Archer DB, & Plaskitt KA (1980) Purification and preliminary characterization of Spiroplasma fibrils. *J Bacteriol* 142(2):694-700.
17. Tulum I, Tahara YO, & Miyata M (2019) Peptidoglycan layer and disruption processes in *Bacillus subtilis* cells visualized using quick-freeze, deep-etch electron microscopy. *Microscopy (Oxf)* 68(6):441-449.

18. Heuser JE (2014) Some personal and historical notes on the utility of "deep-etch" electron microscopy for making cell structure/function correlations. *Mol Biol Cell* 25(21):3273-3276.
19. Shi H, Bratton BP, Gitai Z, & Huang KC (2018) How to build a bacterial cell: MreB as the foreman of *E. coli* construction. *Cell* 172(6):1294-1305.
20. Zivanov J*, et al.* (2018) New tools for automated high-resolution cryo-EM structure determination in RELION-3. *Elife* 7:e42166.
21. Grant T, Rohou A, & Grigorieff N (2018) cisTEM, user-friendly software for single-particle image processing. *Elife* 7:e35383.
22. Lee JE, Cornell KA, Riscoe MK, & Howell PL (2001) Structure of *E. coli* 5'-methylthioadenosine/S-adenosylhomocysteine nucleosidase reveals similarity to the purine nucleoside phosphorylases. *Structure* 9(10):941-953.
23. Nakane D, Ito T, & Nishizaka T (2020) Coexistence of two chiral helices produces kink translation in *Spiroplasma* swimming. *J Bacteriol* 202(8):e00735-00719.
24. Boudet JF*, et al.* (2018) Large variability in the motility of spiroplasmas in media of different viscosities. *Sci Rep* 8(1):17138.
25. Garnier M, Clerc M, & Bove JM (1984) Growth and division of *Spiroplasma citri*: elongation of elementary helices. *J Bacteriol* 158(1):23-28.
26. Parveen N & Cornell KA (2011) Methylthioadenosine/S-adenosylhomocysteine nucleosidase, a critical enzyme for bacterial metabolism. *Mol Microbiol* 79(1):7-20.
27. Fraser CM*, et al.* (1995) The minimal gene complement of *Mycoplasma genitalium*. *Science* 270(5235):397-403.
28. Mizutani M & Miyata M (2019) Behaviors and energy source of *Mycoplasma gallisepticum* gliding. *J Bacteriol* 201(19):e00397-00319.
29. Kinosita Y, Miyata M, & Nishizaka T (2018) Linear motor driven-rotary motion of a membrane-permeabilized ghost in *Mycoplasma mobile*. *Sci Rep* 8(1):11513.
30. Kinosita Y*, et al.* (2014) Unitary step of gliding machinery in *Mycoplasma mobile*. *Proc Natl Acad Sci U S A* 111(23):8601-8606.
31. Uenoyama A & Miyata M (2005) Gliding ghosts of *Mycoplasma mobile*. *Proc Natl Acad Sci U S A* 102(36):12754-12758.
32. Trachtenberg S, Schuck P, Phillips TM, Andrews SB, & Leapman RD (2014) A structural framework for a near-minimal form of life: mass and compositional analysis of the helical mollicute *Spiroplasma melliferum* BC3. *PLoS One* 9(2):e87921.
33. Ku C, Lo WS, & Kuo CH (2014) Molecular evolution of the actin-like MreB protein gene family in wall-less bacteria. *Biochem Biophys Res Commun* 446(4):927-932.
34. Egan AJF, Errington J, & Vollmer W (2020) Regulation of peptidoglycan synthesis and remodelling. *Nat Rev Microbiol* 18(8):446-460.
35. Fu G*, et al.* (2018) MotAB-like machinery drives the movement of MreB filaments during bacterial gliding motility. *Proc Natl Acad Sci U S A* 115(10):2484-2489.

497 36. Terahara N, Tulum I, & Miyata M (2017) Transformation of crustacean
498 pathogenic bacterium *Spiroplasma eriocheiris* and expression of yellow
499 fluorescent protein. *Biochem Biophys Res Commun* 487(3):488-493.
500 37. Uenoyama A, Kusumoto A, & Miyata M (2004) Identification of a 349-
501 kilodalton protein (Gli349) responsible for cytadherence and glass binding
502 during gliding of *Mycoplasma mobile*. *J. Bacteriol.* 186:1537-1545.
503 38. Nishikawa MS*, et al.* (2019) Refined mechanism of *Mycoplasma mobile*
504 gliding based on structure, ATPase activity, and sialic acid binding of
505 machinery. *mBio* 10(6):e02846-02819.
506 39. Zhang K (2016) Gctf: Real-time CTF determination and correction. *J Struct*
507 *Biol* 193(1):1-12.

508

Table 1. Dimensions of cell and ribbon

Parameters	Negatively stained electron microscopy	Quick-freeze, deep-etch electron microscopy	Optical microscopy
Cell thickness (a)	196 ± 26 nm	179 ± 23 nm	
Ribbon width (b)	147 ± 24 nm	118 ± 17 nm	
Cell helical pitch (c)	696 ± 73 nm	706 ± 43 nm (LH)	696 ± 32 nm (LH) 697 ± 37 nm (RH)
Ribbon 1/2 helical pitch (d)	348 ± 44 nm	350 ± 30 nm (LH)	
Ribbon helical pitch (e)	684 ± 60 nm	700 ± 60 nm (LH)	
Ribbon helical diameter (f)	137 ± 30 nm	118 ± 17 nm	
Cell helical diameter (g)	383 ± 45 nm	310 ± 26 nm	
Isolated ribbon pitch	350 ± 17 nm		
Isolated fibril pitch	343 ± 22 nm	351 ± 34 nm (LH)	

*, ** $p > 0.05$ (the agreements between cell pitch and ribbon pitch were supported by Student's *t*-test)

Table 2. Protein components of isolated ribbon.

Protein band	Gene ID	Annotation	MW (kDa)	Density ratio (%)	
				A22 untreated	A22 treated
(i)	SPE-1201	Hypothetical protein	85.8	4	5
(ii)	SPE-0013	FtsH	77.0	12	17
(iii)	SPE-0666	Fibril	58.7	47	67
(iv)	SPE-1231	MreB5	38.5	10	7
(v)	SPE-1224 SPE-1230	MreB2 MreB4	37.8 40.7	27	4

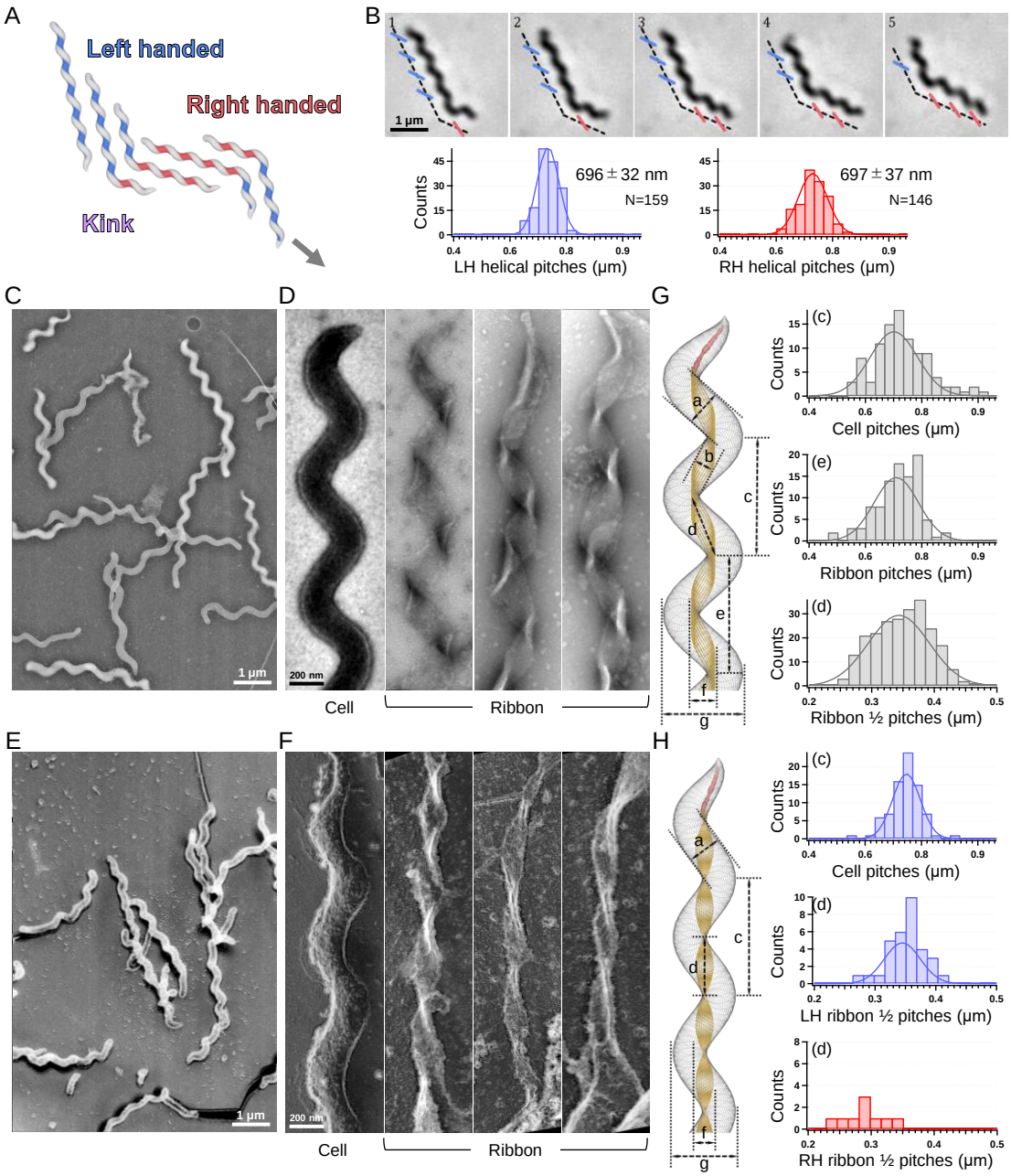

Figure 1. Cell helicity derived from the ribbon structure. (A) Schematic of helicity-switching swimming. The swimming direction is indicated by an arrow. (B) Phase-contrast microscopy of swimming cell. The blue and red segments indicate the left- and right-handed helicity, respectively (upper). Histograms of both left- and right-handed helical pitches of swimming cells, fitted by Gaussian curves with peak tops of 696 ± 32 and 697 ± 37 nm, respectively (lower). (C, E) Field image of cells acquired by negative-staining and quick-freeze, deep-etch (QFDE) electron microscopy (EM). (D, F) Intact cells (leftmost) and ribbons prepared on grids (others). (G, H) Dimensions marked in cell schematics (a)-(g) (left) are summarized in histograms (right) and Table 1.

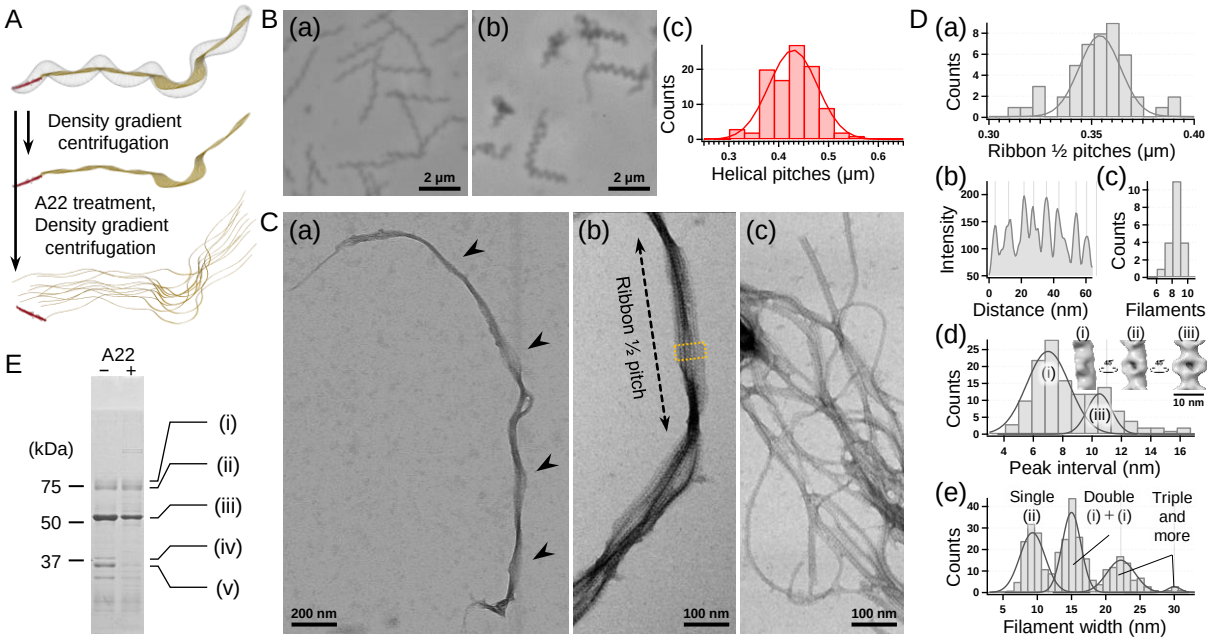

Figure 2. Isolation and characterization of ribbon. (A) Schematic for isolation and disassembly of ribbon. (B) Effects of A22 on swimming cells. (a) Untreated. (b) A22-treated for 2 min. (c) Histogram of the helical cell pitches after A22 treatment, fitted by a Gaussian curve with a peak at 426 ± 47 nm. (C) Electron microscopy (EM) observation of isolated ribbon fractions. (a) The whole structure of the isolated ribbon with helicity as shown by periodical wide positions (marked by arrows). (b) The magnified image of the isolated ribbon and the helical pitch is indicated by a bidirectional arrow. (c) Disassembled ribbon comprising protofilaments. (D) Numerical characterization. (a) Histogram for the helical pitches of the isolated ribbon, fitted by a Gaussian curve with a peak at 351 ± 16 nm. (b) Sectional image profile of the area boxed in panel (C-b). The peaks correspond to the center of the protofilament. (c) Histogram for the number of protofilaments involved in a ribbon. (d) Histogram for the protofilament width in ribbons. The distribution can be fitted by two Gaussian curves marked (i) and (ii), with peaks around 7.0 and 10.5 nm, respectively. (Inset) The images of the reconstituted structures viewed from different angles (refer to Fig. 4). (e) Histogram for the width of the protofilament in disassembled ribbons, fitted with three Gaussian curves with peak tops of 9.5, 15, 22.2, and 30.1 nm. (E) SDS-10% PAGE of the ribbon fraction isolated from original and A22-treated cells.

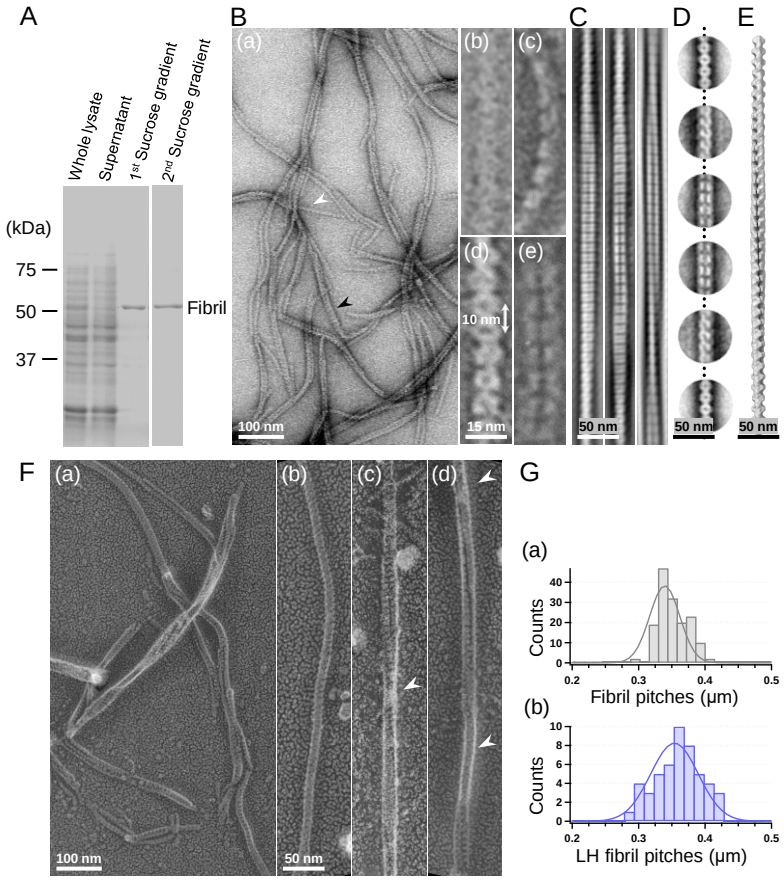

Figure 3. Helical pitches of the isolated fibril filament. (A) Protein profiles of fractions in purification process for fibril protein. (B) Purified fibril filaments observed by negative-staining electron microscopy (EM). (a) Field image. White and black arrows indicate single and double strands, respectively. (b, c) Front and side views of the single-stranded fibril filaments. (d, e) Front and side views of the double-stranded fibril filaments. (C) Double stranded filaments reconstituted through Fourier transformation. (D) Averaged images of double-stranded filaments reconstructed from 62, 11, and 23 images, respectively, for the topmost, second, and third panels. Repeated alignment of three images shown for comparison with panel (C). (E) Model for the double-stranded fibril filament (Refer to Fig. 4). (F) Fibril filaments observed by quick-freeze, deep-etch (QFDE)-EM. Field (a), single-stranded filament (b), and double-stranded filaments (c, d) are presented. (G) Histograms of the helical pitches for the fibril filaments measured for negative-staining (a) and QFDE (b) EM observations. Pitches were fitted by Gaussian curves with peaks at 343 ± 22 and 351 ± 34 nm.

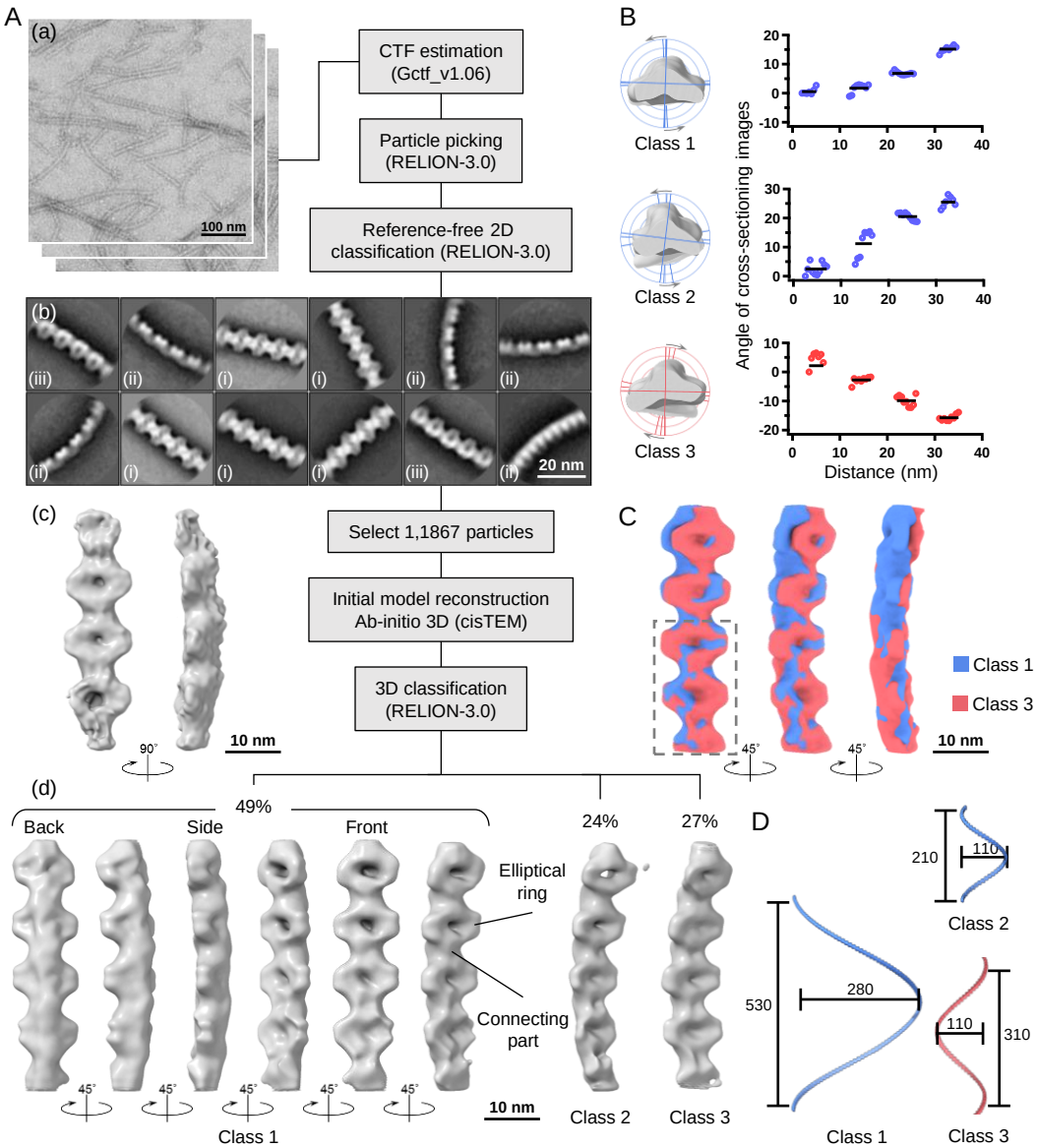

Figure 4. Three-dimensional reconstruction of fibril filaments. (A) Workflow of single particle analysis using negative-staining electron microscopy (EM). (a) Single-stranded fibril filaments prepared by sonication. (b) Averaged images by “2D classification.” (c) Initial 3D model generated by *ab-initio* reconstruction of cisTEM software. (d) Three different conformations of the fibril filament reconstituted by “3D classification.” (B) Rotation of repeated units along the filament axis. Feret diameter angles for the cross-sectional images were plotted along the filament in positions with a Feret diameter longer than 80% of the filament maximum (right). (C) Superimposition of class 1 (left-handed) and class 3 (right-handed) structures. The fitting reference is indicated by the dashed box. (D) Three types of fibril filament models showing 44 repeated units.

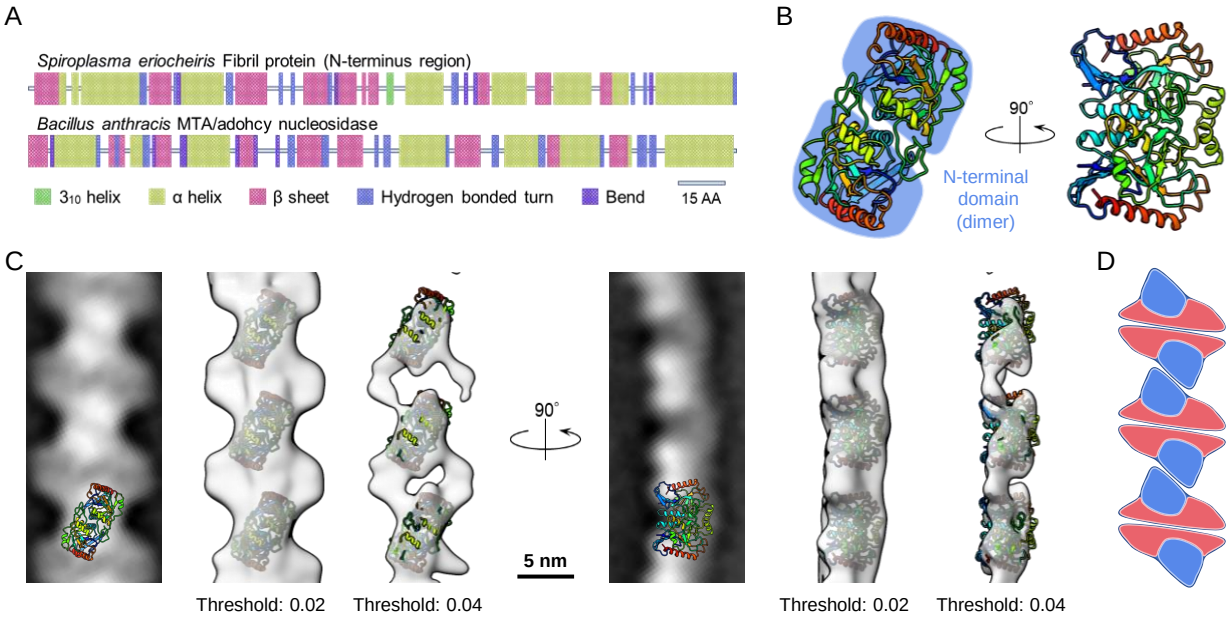

Figure 5. Assignment of predicted fibril protein structure to density map. (A) Comparison of the secondary structure predicted from amino acid sequences of the N-terminal region of fibril protein (upper) and methylthioadenosine/S-adenosylhomocysteine (MTA/SAH) nucleosidase of *Bacillus anthracis* (lower). (B) Predicted structure for N-terminal domain of fibril protein. The structure was predicted as a homodimer as marked by the blue background in the left image. (C) Alignment of predicted structure to density map. Two-dimensional averaged image (left in each) and fitting of N-terminal domain to density map of different thresholds (middle and right, in each) are viewed from two angles apart by 90 degrees. (D) Assignments of N-terminal (blue) and C-terminal (red) domains in the fibril filament.

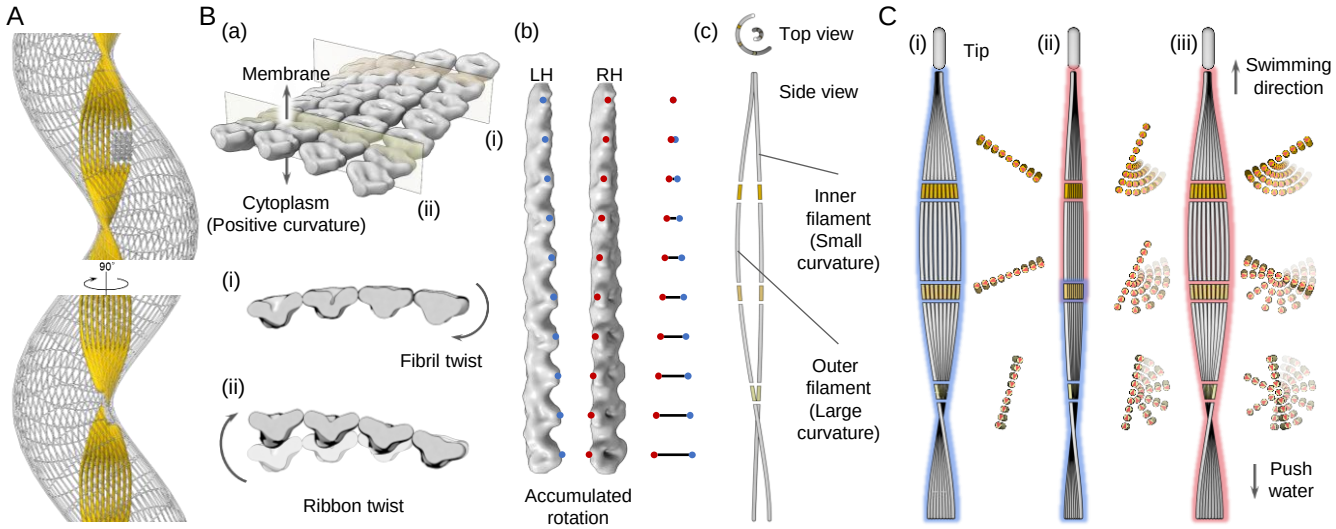

Figure 6. Model schematic for swimming. (A) Ribbon alignment along innermost line of helical cell body. (B) Relation between helicity of fibril filament and ribbon. (a) The ribbon comprises fibril filaments. Cross sections of the ribbon at positions (i) and (ii) are shown in lower panel. The filaments show positive curvature to the cytoplasmic side. The twists of individual fibril filaments result in the twist of the whole ribbon because the filaments bind to the neighboring filaments through their fixed positions. (b) The twist of the fibril filament accumulated through the stack of units. The horizontal positions of oval ends are shown for each unit. The positional difference of the end points is shown by lines between the red and blue dots. (c) Curvatures of the protofilament. For ribbon formation, each protofilament should take a different curvature. (C) Helix rotation caused by the accumulated twist (Movie_S3). The whole and small stack of ribbons are presented, respectively, in left and right, for each of three conformations (i), (ii), and (iii). The ribbon is stabilized by a “Tip” at the front end. The left-handed ribbon (i), the transition state of the ribbon from left-handed to right-handed by helicity-switching, with a switch point traveling from front to back (ii), and the resultant right-handed ribbon (iii) are presented. The left-handed and right-handed areas are marked by blue and red outlines, respectively. Rotation of small stacks from conformation (i) are presented by traces with transition from light to deep colors. The twist of the ribbon accumulates with the switch traveling. The rotations caused by the accumulated twist pushes water backward, resulting in the propelling force.